


Hot Deformation and Recrystallization Mechanisms in a Coarse-Grained, Niobium Stabilized Austenitic Stainless Steel (316Nb)



A. HERMANT, E. SUZON, P. PETIT, J. BELLUS, E. GEORGES, F. CORTIAL, M. SENNOUR, and A.-F. GOURGUES-LORENZON 

The hot deformation behavior and associated microstructural evolution of a coarse-grained Nb-bearing austenitic stainless steel (316Nb) has been investigated by the means of torsion tests at high temperature [1223 K to 1423 K (950 °C to 1150 °C)] followed by microstructural characterization. The starting microstructure was varied by applying prior annealing. Except for strains below 10 pct, the resistance to viscoplastic flow is not sensitive to the starting microstructure. On the other hand, prior annealing at higher temperatures increases the resistance to incipient viscoplastic flow and strongly impedes dynamic and post-dynamic recrystallization by delaying the grain boundary bulging phenomenon. It also affects the static recrystallization behavior during further annealing. The influence of the amount of available niobium atoms, in particular close to grain boundaries, is discussed.

<https://doi.org/10.1007/s11661-018-05103-x>

© The Minerals, Metals & Materials Society and ASM International 2019

I. INTRODUCTION

DUE to their excellent corrosion resistance and appropriate combination of mechanical properties at high temperatures, austenitic stainless steels are widely used in chemical, oil and nuclear industries.^[1,2] Ni-Cr-Mo AISI 316-type austenitic stainless steel grades are of particular use in vessels under high operating temperatures and pressures.^[2] Obtaining a homogeneous microstructure in heavy components requires deep understanding of their hot deformation behavior and underlying physical mechanisms. The hot workability of these steels is governed by the competition between work hardening, dynamic recovery (DRV), and dynamic recrystallization (DRX).^[3] Post-dynamic recrystallization (post-DRX) and static recrystallization (SRX) can induce further metallurgical evolution during

cooling and further annealing, respectively.^[4] Competition between all of these mechanisms strongly relies on the particular steel chemistry and on deformation conditions.

The stacking fault energy (SFE) governs the dislocation mobility and recrystallization mechanisms.^[5–7] At room temperature, Mo-containing 316-type austenitic stainless steels present relatively high SFE $> 50 \text{ mJ m}^{-2}$.^[6] In such medium-SFE materials, recovery is promoted prior to recrystallization, by dislocation climb and cross-slip leading to dislocation annihilation or subgrain formation.^[8,9] Annihilation and spatial re-arrangement of dislocations decrease the energy stored in the deformed material. The onset of recrystallization is therefore delayed.^[8] Conversely, austenitic stainless steels with lower SFE, such as Mo-free AISI 304 (SFE $\sim 20 \text{ mJ m}^{-2}$),^[6] show little recovery due to highly dissociated dislocations.^[8,10,11] DRX and SRX mechanisms by nucleation and growth of new dislocation-free grains are therefore dominant in these steels.^[12,13] Although this is scarcely documented in literature, it is worth noting that the SFE generally increases with temperature,^[14–17] which could affect the competition between recovery and recrystallization.

Besides their effect on the SFE, solute elements such as Mo affect recrystallization mechanisms in AISI 316 austenitic stainless steel.^[18,19] Carbide-forming Mo may induce a solute drag effect which clearly delays the DRX and SRX kinetics in comparison to Mo-free AISI 304 steels.^[18,20] Another element widely used to control recrystallization kinetics of steels is niobium. At

A. HERMANT is with MINES ParisTech, PSL Research University, MAT-Centre des Matériaux, UMR CNRS 7633, BP 87, 91003 Evry Cedex, France and also with CEA-Centre de Valduc, 21120 Is sur Tille, France. E. SUZON is with CEA-Centre de Valduc, 21120 Is sur Tille, France. P. PETIT, J. BELLUS, and E. GEORGES are with Aubert & Duval-Usine des Ancizes, 63770 Les Ancizes, France. F. CORTIAL is with Naval Group Research-CESMAN, 44340 Bouguenais, France. M. SENNOUR and A.-F. GOURGUES-LORENZON are with MINES ParisTech, PSL Research University, MAT-Centre des Matériaux, UMR CNRS 7633, BP 87, 91003 Evry Cedex, France. Contact e-mail: anne-francoise.gourgues@mines-paristech.fr

Manuscript submitted July 4, 2018.

Article published online January 8, 2019

moderate hot-working temperatures, Nb can be present as fine Nb-rich carbonitrides leading to grain boundary pinning^[19,20] that also impedes DRX and SRX of microalloyed steels.^[21] The maximum grain boundary pinning effect was reported for particles sizes below 20 nm.^[20] On the other hand, particle-stimulated nucleation (PSN) of new grains may occur at coarser Nb-rich particles that form at the end of solidification.^[22] Whatever the location of Nb atoms, DRV might occur efficiently in Nb-bearing austenite.

The hot deformation behavior of Nb-free 316-type stainless steel has been widely reported.^[2-4] The effect of coarser initial grain size on the DRX, post-DRX and SRX behavior has already been well characterized. The reduction of available nucleation sites by decreasing the grain boundary area per unit volume is responsible for the decrease in DRX and SRX kinetics.^[23] On the other hand, little has been reported on the effect of Nb addition to 316-type steels,^[5] leading to a Nb + Mo bearing steel of the 316 family, called “316Nb” hereafter. As a result, the combined effects of Mo and Nb on recrystallization mechanisms are still not clear yet. In addition, the effect of very coarse initial grain size, higher than 100 μm , coupled to typical hot deformation conditions of heavy components, such as low amounts of strain, low strain rates, and wide range of deformation temperatures on recrystallization mechanisms is not well known in austenitic stainless steels, and in particular in 316Nb. The present work focuses on the recovery/recrystallization behavior of a 316Nb austenitic stainless steel under hot deformation conditions typical of heavy components, as well as during slow cooling and further annealing. A preliminary study focused on a limited set of conditions can be found elsewhere.^[24]

II. MATERIALS AND EXPERIMENTAL DETAILS

A. Materials

A 316Nb austenitic stainless steel (18–20Cr, 12–13Ni, 2.5–2.7Mo, < 2Mn, 0.3–0.5Si, < 0.1C, < 0.05N and 0.5–1.0Nb, all in wt. pct) was provided as hot torsion blanks cut from a forged billet with a fraction of delta ferrite lower than 1 pct. The effects of grain size and initial amount of dissolved Nb were investigated by preparing three starting microstructures using a preliminary heat treatment (denoted as “preconditioning” hereafter). The first two starting microstructures were produced by solution anneal, namely, for 1 hour at 1373 K (1100 °C) (T1) and 1473 K (1200 °C) (T2), respectively, to get a fully recrystallized grain structure and an average grain size D_0 of 130 and 250 μm , respectively. No pronounced crystallographic texture was found by X-ray diffraction. To distinguish the effect of coarser initial grain size from that of higher equilibrium niobium solute content in T2 compared to T1, a specific microstructure (T21) was designed by first soaking at 1473 K (1200 °C) for 1 hour to get a value of D_0 similar to that of T2, then slowly cooling and soaking at 1373 K (1100 °C) for another 1 hour to get the same equilibrium

amount of dissolved Nb as for T1. Preconditioning treatments and corresponding microstructural features are reported in Table I. In this work, the majority of tests were performed on T1 that was considered as the reference microstructure.

B. Hot Torsion Tests

Cylindrical specimens with a gage length of 22 mm and a gage diameter of 6 mm were machined from the preconditioned blanks, and then tested on a computerized hot torsion machine. They were deformed from 0.1 to 0.8, at surface strain rates in the range of 5×10^{-3} to $5 \times 10^{-1} \text{ s}^{-1}$ and at various temperatures from 1223 K to 1423 K (950 °C to 1150 °C). For each test, the specimen temperature was controlled using one thermocouple inserted in one specimen end; another thermocouple was attached to the gauge section of the specimen. The measured difference between the bulk and the surface temperatures of the specimens was lower than 6 K. The full thermal-mechanical cycle is schematically shown in Figure 1. For deformation temperatures lower than 1373 K (1100 °C), the torsion specimens were reheated at $3 \text{ K}\cdot\text{s}^{-1}$ up to about 1323 K (1050 °C) then at $0.15 \text{ K}\cdot\text{s}^{-1}$ up to 1373 K (1100 °C), and then held for 600 seconds in order to dissolve any secondary niobium-rich precipitates that could remain in the starting microstructure. The holding time was short enough to avoid any significant grain growth. Then, the specimens were held for 60 seconds at the deformation temperature for thermal homogenization before being deformed. Right after deformation, they were either water quenched to freeze the microstructure and focus on dynamic phenomena (T1 microstructure only) or slowly cooled down, with a cooling rate of $0.15 \text{ K}\cdot\text{s}^{-1}$ to study non-isothermal post-dynamic phenomena that could occur on heavy components (T1, T2, and T21 microstructures). A further annealing treatment at a unique temperature, T_{anneal} , for 2 hours with a slow heating rate was then applied to one half of every torsion specimen, in order to investigate static phenomena. The value of T_{anneal} was set between 1323 K and 1373 K (1050 °C and 1100 °C) to ensure dissolution of embrittling Cr-rich sigma phase particles that form during slow cooling after hot working. Both hot torsion and annealing cycles were conducted under argon atmosphere. The values of Von Mises equivalent true stress (σ) and true strain (ϵ) were obtained from torque-angle data using the methodology proposed by Fields and Backofen.^[25]

C. Microstructural Investigations

All microstructural observations were carried out in a plane parallel to the specimen axis, by polishing the gauge part down to the effective radius of $2.7 \pm 0.1 \text{ mm}$. The strain experienced in the observed plane ranged from 90 to 100 pct of the surface strain. Homogenous microstructures were observed all over the observed plane, so that strain and strain rates reported in the following are those associated to the surface of cylindrical specimens.

Table I. The Three Investigated Starting Microstructures and Corresponding Solution Anneal Heat Treatments

| Starting Microstructure | Solution Anneal (Preconditioning) Applied to Produce the Microstructure | Average Grain Size (Optical Microscopy) (μm) | Equilibrium Nb Content in Solid Solution (End of Preconditioning) (ThermoCalc®—TCFe7 Database) for 0.5 and 1.0 wt pct Nb in the Average Chemical Composition, Respectively (Wt Pct) |
|-------------------------|---|---|---|
| T1 | 1373 K (1100 °C) for 1 h, air quench | 130 | 0.054 and 0.170 |
| T2 | 1473 K (1200 °C) for 1 h, air quench | 250 | 0.184 and 0.328 |
| T21 | 1473 K (1200 °C) for 1 h, slow cooling down to 1373 K (1100 °C), 1 h, then air quench | 280 | 0.054 and 0.170 |

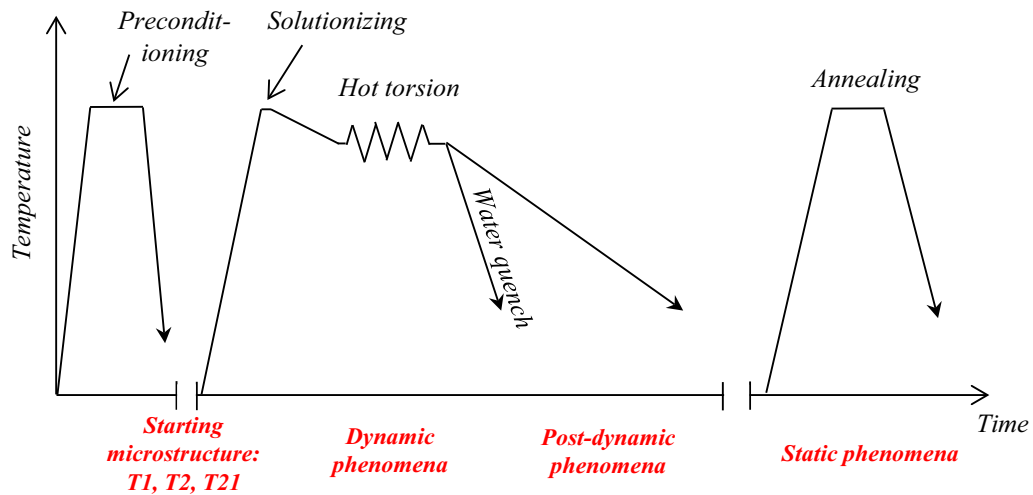


Fig. 1—Schematic view of the full thermomechanical cycle and associated investigated phenomena.

For optical examination of grain size and shape, specimens were polished and electrolytically etched in a 50 pct HNO_3 solution. After a colloidal silica finish, grain and twin boundaries, as well as internal misorientations were determined by electron backscatter diffraction (EBSD) in a FEI Nova NanoSEM 450® scanning electron microscope under an accelerating voltage of 15 kV, using a working distance of 14 mm, a tilt angle of 70 deg and a typical step size of 1.2 μm to avoid missing small recrystallized grains. EBSD data were acquired and analyzed using an EDAX-AMETEK OIM 7® system fitted to a Hikari® camera. For each sample, the typical size of EBSD maps was 0.64 mm^2 . Prior to any analysis a grain dilation noise reduction was applied to each individual dataset using a 2 deg tolerance angle and five pixels for the minimum grain size. Even if some work-hardening left by polishing scratches remained in some of the maps, the percentage of points changed in the noise reduction process was below 1 pct confirming high reliability of the data. General features of the microstructure were observed by combining the pattern quality map (in grey levels) and an inverse pole figure (IPF) color coding according to the sample normal, namely, the radial direction of the torsion specimen.

Recrystallized fractions were calculated from EBSD data by using a grain orientation spread (GOS) criterion. The GOS was calculated as the average misorientations between any pixel of a given grain and the average orientation of that grain.^[26] This value rises for increasingly deformed microstructures due to a high density of geometrically necessary dislocations. The threshold value used to define a recrystallized grain may be as low as 1 deg for austenitic stainless steels.^[27] In the present case, the GOS criterion was set from preliminary EBSD characterizations of the fully recrystallized T1 microstructure. Local orientation gradients attributed to deformation incompatibilities were characterized using kernel average misorientation (KAM) maps, where each pixel was assigned the average disorientation of that pixel with its third neighbors of the same grain. The departure of twin boundaries from the $\Sigma 3$ coincidence was also examined. For microstructures strained by more than 0.2, grains having a GOS ranging between 1 and 2 deg did not exhibit any region where the KAM exceeded 0.5 deg; twin boundaries in these grains did not depart from the $\Sigma 3$ coincidence. Grains with a GOS higher than 2 deg clearly evidenced subboundaries in the KAM maps, as thin regions with $\text{KAM} > 0.5$ deg and as will be shown later, twin boundaries were found to

depart from the $\Sigma 3$ coincidence. Therefore, a threshold value of $\text{GOS} = 2$ deg was considered as most suitable to define a recrystallized grain. For samples deformed up to 0.2, in some cases the grains having a GOS value between 1 and 2 deg also exhibited regions of localized misorientations from the KAM maps. In that case, the critical GOS value was set to 1 deg. Due to the high initial grain size, together with the small size of recrystallized grains at least in the first stages of recrystallization, the EBSD map size was adjusted in order to analyze at least 100 grains per map. From EBSD maps taken from distinct regions in the same samples, the accuracy of determined recrystallized fractions was found to be controlled by sampling effects to a value of 5 pct (absolute value). Some unrecrystallized, but slightly deformed grains could yet be taken as recrystallized according to the $\text{GOS} = 2$ deg criterion, especially for applied strains lower than 0.2. As a consequence, the absolute uncertainty in the values of recrystallized fractions for $\varepsilon = 0.2$ was considered to be 10 pct. In all EBSD maps reported in the present paper, the torsion axis is horizontal.

Carbon extraction replicas were prepared after Villela etching to characterize the distribution of the (Nb,Mo)(C,N) carbonitrides. Dislocation substructures and chemical composition close to grain boundaries were characterized from twin jet-polished thin foils, examined in a FEI TECNAI F20 field emission gun transmission electron microscope (TEM) operated at 200 kV either in conventional TEM mode or in STEM mode combined with an X-ray energy-dispersive spectrometer (EDS). Fine carbonitrides were found to be of the MX type, where M denotes metallic elements. From local EDS analysis in the TEM, the metallic part of the MX chemistry contained 5 to 10 wt pct Mo, less than 3 pct Cr, and more than 85 pct Nb. As these precipitates formed from the solid solution after the preconditioning treatment, and in view of the solubility of Mo, Nb and Cr in carbon-containing austenite, only the amounts of Nb (and C) in solid solution were considered to significantly vary with the preconditioning treatment. The amounts of Mo and Cr in solid solution were considered similar in all microstructures.

III. RESULTS

A. Flow Behavior

From hot torsion tests up to various amounts of strain, the reproducibility of flow curves was better than 5 MPa and the flow curves obtained under given strain rate and deformation temperature were parallel to each other, showing remarkable reproducibility of the strain hardening behavior. Representative flow curves obtained for different temperatures and strain rates for an initial grain size of 130 μm (T1) are shown in Figure 2. They are close to those reported for 316-type steel deformed in similar conditions.^[28,29] As expected, the flow stress increased with decreasing the deformation temperature and increasing the strain rate (Figure 2(a)). At $5 \times 10^{-2} \text{ s}^{-1}$, the flow curves exhibited

a yield point for deformation temperatures of at least 1323 K (1050 °C), more readily visible in Figure 2(b). Such a yield point was also visible (but not commented) on coarse-grained nickel-based superalloy René88 when deformed above the solvus temperature of γ' precipitates.^[30] In the present work, decreasing the strain rate down to $5 \times 10^{-3} \text{ s}^{-1}$ led to a yield point even at lower deformation temperatures. The strain rate sensitivity parameter was around 0.12 to 0.14 for the investigated conditions, in agreement with the 0.06 to 0.17 interval reported by Wenhui *et al.*^[31] on a so-called “Nb-bearing” 316LN stainless steel.

From the experimental curves of Figure 2, the flow stress gradually increased in the work-hardening regime due to interaction between dislocations. Over the range studied (amount of strain up to 0.8), it reached a single maximum σ_p at a peak strain ε_p between 0.5 and 0.6 whatever the deformation conditions. Then, it slightly decreased in the softening regime that was supposed to be associated to the development of strain-free grains by DRX.^[31] Although a single peak behavior is generally associated to high strain rates and low deformation temperatures, the relative grain size D_0/D_s , where D_s is the stable DRX grain size and D_0 is the initial grain size, can also control the shape of the flow curve.^[9] In the investigated coarse-grained microstructures, the grain refinement DRX regime was predominant, recrystallization was expected to be heterogeneous, consistently with the observed single peak in the flow curves of Figure 2.

To estimate the critical strain, ε_c for the onset of DRX as in *e.g.*, Reference 3 the logarithm of the work hardening rate parameter, $\ln(d\sigma/d\varepsilon)$ was plotted as a function of the equivalent stress, σ . In such plots, the inflexion point close to the peak stress, σ_p indicated the critical stress, σ_c ^[3] and the associated critical strain ε_c was then derived using the flow curve. A value of $\varepsilon_c \approx 0.3$ was found for most of the experiments conducted. The relationship $\varepsilon_c \approx 0.6 \times \varepsilon_p$ well agreed with previous reports of the recrystallization behavior of austenite (*e.g.*, References 3, 4, 32, and 33). In the present work, except at high deformation temperature and low strain rate (1423 K (1150 °C) and $5 \times 10^{-3} \text{ s}^{-1}$, see Figure 2(a)), the estimated critical strain did not markedly depend on deformation conditions.

To quantitatively describe the dependence of peak stress σ_p on applied strain rate and deformation temperature T_ε , an empirical equation expressing the flow rate $\dot{\varepsilon}$ as a function of σ_p and T_ε was determined as first proposed by Sellars and McTegart^[34]:

$$\dot{\varepsilon} = A[\sinh(\alpha\sigma_p)]^n \exp(-Q/RT_\varepsilon). \quad [1]$$

In Eq. [1], A and α are material constants, n is the stress exponent, Q is the apparent activation energy, and R is the gas constant. The parameters of Eq. [1] were adjusted for the reference T1 microstructure, for which the experimental database was the largest one. The values of parameters were obtained through linear regression from experimental data as in References 34 and 36. The values of σ_p estimated using Eq. [1] and these calibrated parameters did not differ from

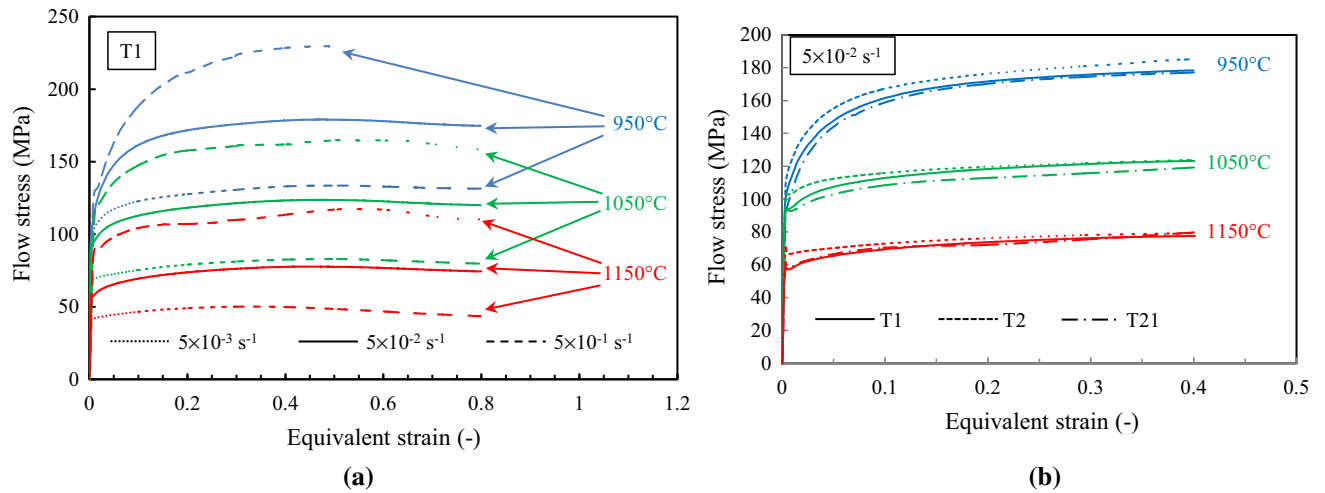


Fig. 2—Stress–strain curves from hot torsion tests at various temperatures (a) of the T1 microstructure at various strain rates and (b) of the three microstructures at $5 \times 10^{-2} \text{ s}^{-1}$.

Table II. Experimental Values of Peak Stress Obtained for the T1 Microstructure and Compared to Those Predicted by Eq. [1]

| Strain rate | $5 \times 10^{-3} \text{ s}^{-1}$ | | $5 \times 10^{-2} \text{ s}^{-1}$ | | $5 \times 10^{-1} \text{ s}^{-1}$ | |
|-------------------------|-----------------------------------|--------------|-----------------------------------|--------------|-----------------------------------|--------------|
| | Measured | From Eq. [1] | Measured | From Eq. [1] | Measured | From Eq. [1] |
| Deformation Temperature | | | | | | |
| 1223 K (950 °C) | 137 | 135 | 184 | 182 | 229 | 231 |
| 1323 K (1050 °C) | 85 | 85 | 124 | 122 | 165 | 166 |
| 1423 K (1150 °C) | 52 | 53 | 81 | 80 | 117 | 116 |

Table III. Comparison Between Parameter Values of Eq. [1] and Those Reported in Literature for Austenitic Stainless Steels Deformed in Similar Conditions

| Material | $A \text{ (s}^{-1}\text{)}$ | $1/\alpha \text{ (MPa)}$ | n | $Q \text{ (kJ/mol)}$ | References |
|---------------------------|-----------------------------|--------------------------|------------|----------------------|--------------|
| AISI 316 | (not reported) | 83 | 3.9 to 4.5 | 393 | 32 |
| AISI 316LN | 1.54×10^{16} | 118 | 4.7 to 5.7 | 459 | 1 |
| AISI 316LN | 1.139×10^{15} | 127 | 5.33 | 421 | 35 |
| 0.05Nb bearing AISI 316LN | 3.23×10^{19} | 173 | 6.83 | 518 | 31 |
| 316Nb | 7.2×10^{14} | 100 | 4.93 | 433 | present work |

measured ones by more than 2.5 pct (Table II). The value of Q obtained in the present study agrees with most of literature data reported in Table III. It also agrees with that reported for viscoplastic deformation of 316-type austenitic stainless steel (414 to 485 kJ/mol^[1]); it is slightly higher than that reported for Mo-free type 304 austenitic stainless steel (370 to 415 kJ/mol^[37,38]). More generally, the values of parameters found in this work are in good agreement with those reported on 316 grade steels (Table III).

Figure 2(b) shows representative flow curves up to $\varepsilon = 0.4$, for a constant strain rate of $5 \times 10^{-2} \text{ s}^{-1}$ as a function of the starting microstructure. Whatever the test temperature, the T2 microstructure exhibited a slightly higher flow stress than T1 and T21 at incipient plasticity. For the test temperatures of 1223 K (950 °C) and 1423 K (1150 °C), the flow curves of T1 and T21 microstructures were very similar, whereas the T2

microstructure possessed the highest flow stress. The work hardening rate of T2 was significantly lower than that of T1 at 1423 K (1150 °C), this difference decreasing with decreasing the test temperature. At 1323 K (1050 °C), the difference in flow stress between T1 and T2 (90 and 104 MPa at $\varepsilon = 0.01$, respectively) decreased during deformation to almost vanish at $\varepsilon = 0.4$ (120 and 123 MPa, respectively), *i.e.*, before reaching the peak stress. The work hardening ability appeared lowest for the T2 microstructure. At this temperature, the flow behavior of T21 appeared intermediate between those of T1 and T2. Therefore, for a given equilibrium amount of Nb in solid solution at the end of preconditioning (T1 vs T21), increasing the (coarse) average grain size from 130 μm up to 280 μm did not significantly affect the flow properties, except at 1323 K (1050 °C). By comparing T2 and T21 (similar grain size, see Table I), increasing the equilibrium amount of Nb in solid solution

significantly changed the hardening behavior by a rise in yield stress and a decrease in work hardening ability. For amounts of equivalent strain higher than about 0.3, the flow stress was fairly independent of the starting microstructure (Figure 2(b)); so that the parameters of Eq. [1] reported in Table III also correctly describe the resistance of T2 and T21 microstructures to viscoplastic flow.

B. Microstructural Investigation of Dynamic Phenomena in the T1 Microstructure

1. Phenomenology

Typical microstructures developed after deformation of T1 specimens at 5×10^{-2} and 5×10^{-3} s⁻¹ followed by water quenching are shown in Figure 3. The material displays some straight deformation bands (region A in Figure 3(a)) characteristic of planar slip of dislocations commonly observed in low SFE materials. Strain localization and stress concentration were therefore potentially important next to grain and twin boundaries. As a result, grain boundaries dynamically evolved at low strain and high temperature (region B in Figure 3(a)). From EBSD pattern quality close to these serrated grain boundaries, subgrain boundaries appeared as a result of DRV (Figures 3(a) and (b)). At higher strains they eventually closed by geometrically necessary dislocations by the mechanism described in Reference 10 and transformed into low angle boundaries (Figure 3(c)). Subgrains with similar crystallographic orientation as the initial grain were thus created close to grain boundaries as reported in Reference 8. The same microstructural evolution under hot deformation has already been well documented for 304 and 316-type steels.^[4,13,35,39,40] It is thus not solely due to the presence of Mo or Nb. A similar bulging phenomenon was also reported in coarse-grained Ni-20Cr,^[41] Ni-(0 to 20)Fe,^[42] Ni-30Fe-(C, Nb)^[43] as well as in solid-solution René88 alloy.^[30]

For the strain rate of 5×10^{-2} s⁻¹, decreasing the deformation temperature at given strain level led to less serrated grain boundaries and thus, to less extensive subgrain formation. No grain boundary serration was observed at $\epsilon = 0.1$ whatever the deformation temperature and strain rate, showing a critical deformation between 0.1 and 0.2 to initiate significant grain boundary bulging. No subgrain formation was ever observed close to the serrated grain boundaries for T1 specimens deformed up to $\epsilon = 0.2$ below 1273 K (1000 °C). When the applied strain rose from $\epsilon = 0.2$ up to $\epsilon = 0.8$, subgrain boundary misorientations gradually increased to yield high angle boundaries (Figure 3(c)). New twin-free DRX grains, originated from the DRV subgrains were observed along the former grain boundaries (e.g., in region C of Figure 3(b)), at a strain of 0.4, i.e., lower than the peak strain but consistently with the value of $\epsilon_c \approx 0.3$ estimated from the flow curves. These grains were of a few micrometers in size, which was also the typical size of DRV cells (Figures 3(a) and (b)). At low deformation temperature, below 1273 K (1000 °C), subgrains were readily observed at grain boundaries for $\epsilon = 0.4$ only. Accordingly and in agreement with the flow behavior, a partially recrystallized necklace microstructure was found at $\epsilon > 0.4$. As a whole, the recrystallized fraction did not exceed 5 and 15 pct in T1 specimens that had been water quenched after deformation at 5×10^{-2} s⁻¹, up to $\epsilon = 0.8$ at respectively 1323 K (1050 °C) (region C in Figure 3(b)) and 1423 K (1150 °C).

Dynamic recovery was promoted by decreasing the strain rate down to 5×10^{-3} s⁻¹ (region D in Figure 3(c)). A high density of low angle boundaries was detected in unrecrystallized grains (grey lines in Figure 3(c)). However, at a given strain level and deformation temperature, DRX was also promoted by decreasing the strain rate down to 5×10^{-3} s⁻¹. Due to the higher amount of time spent at high temperature to reach a given strain level, nucleation of small grains at bulged grain boundaries occurred more readily. A

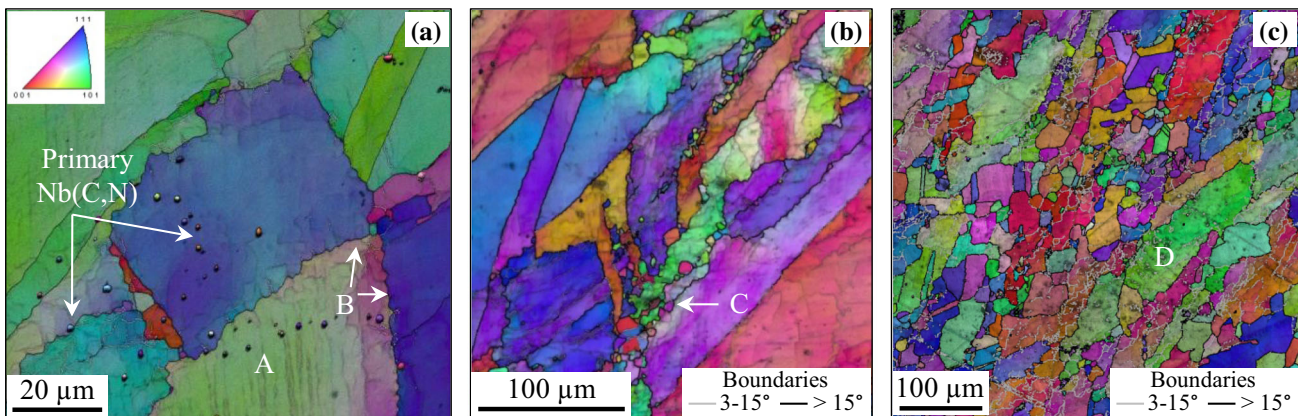


Fig. 3—EBSD map (pattern quality + IPF) from a T1 specimen strained up to (a) $\epsilon = 0.4$ and (b) $\epsilon = 0.8$ at 1323 K (1050 °C) and 5×10^{-2} s⁻¹ then water quenched and (c) from a T1 specimen strained up to $\epsilon = 0.8$ at 1373 K (1100 °C) and 5×10^{-3} s⁻¹ then water quenched. A: straight deformation bands; B: grain boundary bulging; C: small DRX grains nucleated at grain boundaries; D: well-recovered grain. (a) is adapted from Ref. [24].

recrystallized fraction of 15 pct was found for specimens deformed up to $\varepsilon = 0.8$ below 1373 K (1100 °C) at $5 \times 10^{-3} \text{ s}^{-1}$, *i.e.*, the same fraction as that obtained for the same amount of strain at 1423 K (1150 °C) and $5 \times 10^{-2} \text{ s}^{-1}$.

For these hot deformation conditions and starting microstructures, DRX was not the dominant phenomenon in the metallurgical evolution, in contrast to results reported on 304 and 316 austenitic stainless steels.^[31,44] Even at high strains, only a limited fraction of grain boundaries experienced DRX, whereas other boundaries of the same sample did not experience undulations (*e.g.*, Figure 3(c)).

2. Recovery and recrystallization at annealing twin boundaries

It is worth noting that a significant fraction of unrecrystallized grains observed at the end of the hot deformation process were actually twin-free, although the starting microstructure exhibited a high density of annealing twins as usually encountered in recrystallized 316-type steels. Nucleation of small DRX grains at twin boundaries generally occurs once grain boundary nucleation sites have been saturated, as reported by *e.g.*, References 23 and 45 in a 17Cr-14Ni A220 stainless steel, and by Reference 46 in a nickel-based superalloy 718. This actually leads to fragmentation of parent grains that eventually become twin-free.^[23] In the present case, (*e.g.*, Figure 3(b)), twin-free parent grains were found well before saturation of grain boundary nucleation sites. The mechanism leading to disappearance of annealing twins in unrecrystallized grains was therefore further investigated. Figure 4 illustrates two different, but typical local microstructures of the hot deformed material close to annealing twins. White lines represent $\Sigma 3$ grain boundaries, calculated according to the classical Brandon criterion.^[47] As illustrated in Figure 4 and widely reported in literature, most of the twins eventually lost the $\Sigma 3$ coincidence during hot deformation; due to the crystal rotations associated to viscoplastic deformation, annealing twin boundaries

transformed into general high angle boundaries. These eventually became able to migrate more easily by the mechanisms reported in the previous section.

Although the misorientation of nearly all twin boundaries of unrecrystallized grains deviated from the $\Sigma 3$ coincidence after hot deformation (*i.e.* even for rather straight twins such as that in Figure 4(a)), plastic deformation incompatibilities between parent grain and annealing twins actually depended on the locally activated slip systems, *i.e.*, on both the local microtexture and applied loading conditions.

In some cases, as illustrated in Figure 4(a) and also reported in Ni-20Cr by Reference 41, the twin boundaries kept rather smooth and stable even if departing from a $\Sigma 3$ coincidence, indicating a low amount of stored energy close to them. Significant subgrain formation was only observed close to the grain boundary itself, as *e.g.*, on the top part of the twin in Figure 4(a). This suggests that the activated slip systems were common to twin and parent grain, so that plastic deformation could easily be transferred from the parent grain to the twin by dislocation motion. In that case, the twin boundaries remained easily recognizable; distortions only occurred at localized regions (such as the bottom part of the twin boundary of Figure 4(a)). Only gradual crystal rotation induced by geometrically necessary dislocations was observed.

In other cases such as in Figure 4(b), twin boundaries were strongly distorted. In that case, it could be assumed that activated slip systems were not common to twin and parent grains, so that the plastic deformation could not be readily transmitted to the twin and plastic strain incompatibilities accumulated close to the twin boundaries, as illustrated by the highly distorted boundary geometry, the high density of subgrain boundaries and the high average value of KAM in Figure 4(b) compared to Figure 4(a). In that case, serrations appeared at the twin boundaries, *i.e.*, the twin boundaries became unstable. As in the case of general grain boundaries, DRV, then DRX was strongly promoted close to unstable twin boundaries (Figure 4(b)), this specific

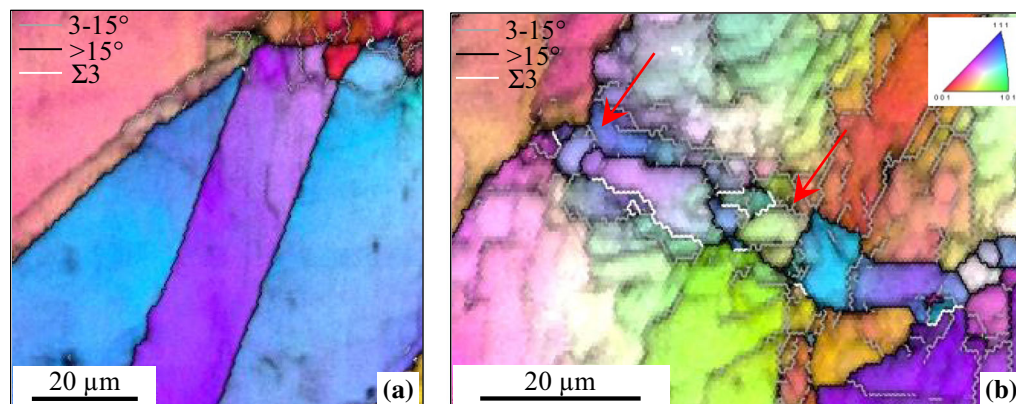


Fig. 4—EBSD maps (pattern quality + IPF) from T1 water quenched sample showing microstructural changes close to (a) a stable twin and (b) an unstable twin after hot deformation up to $\varepsilon = 0.8$ at 1323 K (1050 °C) and $5 \times 10^{-2} \text{ s}^{-1}$. Average values of KAM are 1.0 and 2.5 deg in the two regions, respectively. Close to the arrows in (b), the twin has started to vanish. Both regions are taken from the map of Fig. 3(b). Adapted from Ref. [24].

mechanism leading to a vanishing of either twin or parent grain orientations. In most observed cases, as illustrated in Figure 4(b) (close to the red arrows), the high-angle boundaries disappeared and low-angle boundaries were found, instead, together with a high level of recovery but still elevated values of KAM; no, small, recrystallized grain with low values of KAM was observed in lieu of the existing twin. Only further progress of the bulging mechanism could eventually lead to new, recrystallized grains there. Consequently, the twin orientation gradually disappeared *to the benefit of the parent grain*, resulting in a recovered, non-recrystallized, twin-free grain. In fact, the twin disappeared without fragmenting the parent grain. To the authors' knowledge, this mechanism had not been reported yet in literature.

C. Post-dynamic Phenomena: Microstructural Evolution During Slow Cooling

1. T1 microstructure

From metallographic and GOS measurements, DRX was only restricted to highly strained samples ($\epsilon > 0.2$) and higher deformation temperatures. In most of the studied conditions, the microstructure kept unrecrystallized right after hot deformation but locally showed subgrains at serrated grain boundaries.

Figures 5(a) and (b) display GOS maps after $\epsilon = 0.2$ at 1323 K (1050 °C) and $5 \times 10^{-2} \text{ s}^{-1}$ followed by water quenching and slow cooling, respectively. In all GOS maps reported in the paper, blue and green grains (GOS < 2 deg) correspond to recrystallized grains. No DRX was evidenced from Figure 5(a). As illustrated in Figure 5(b), post-DRX involving subgrain growth at prior grain boundaries was observed in certain conditions. Figure 5(c) summarizes the recrystallization fraction as a function of deformation temperature and amount of strain. In specimens deformed at 1423 K (1150 °C), the recrystallized fraction reached about 0.9 after slow cooling for both values of applied strain. Conversely, in specimens deformed at 1223 K (950 °C), the recrystallized fraction did not exceed 0.02 after slow cooling. After deformation at 1323 K (1050 °C), post-DRX partially occurred but no necklace structure was observed (Figure 5(b)). This could be due to rapid growth of new DRX grains and to incomplete covering of grain boundaries with DRX nuclei. With further increase in strain, the recrystallized fraction originated from post-DRX was significantly higher (see Figures 5(c) and (d) and solid circles in Figure 5(g)). Increasing the deformation temperature up to 1423 K (1150 °C) strongly accelerated post-DRX (Figures 5(e) and (f)). Furthermore, decreasing the strain rate down to $5 \times 10^{-3} \text{ s}^{-1}$ did not influence DRX phenomena but increased the minimum deformation temperature associated to post-DRX. For instance, the fraction of post-DRX grains after a deformation of $\epsilon = 0.4$ at 1323 K (1050 °C) was 0.09, to be compared with 0.43 after the same cycle with a strain rate of $5 \times 10^{-2} \text{ s}^{-1}$ (Figure 5(d)). In contrast to DRX, no specific recrystallization at twin boundaries was observed and unrecrystallized grains were free from destabilized twins, *i.e.*,

Fig. 5—EBSD pattern quality + GOS map showing post-DRX from a T1 specimen deformed up to (a, b) $\epsilon = 0.2$ and (c, d) $\epsilon = 0.4$ at 1323 K (1050 °C) and $5 \times 10^{-2} \text{ s}^{-1}$ then followed by (a, c) water quenching and (b, d) slow cooling. (e, f) EBSD pattern quality + GOS map showing post-DRX from a T1 specimen deformed up to $\epsilon = 0.4$ at 1423 K (1150 °C) and $5 \times 10^{-2} \text{ s}^{-1}$ then followed by (e) water quenching and (f) slow cooling. (g) Recrystallized fraction experimentally measured after deformation at $5 \times 10^{-2} \text{ s}^{-1}$ followed by slow cooling.

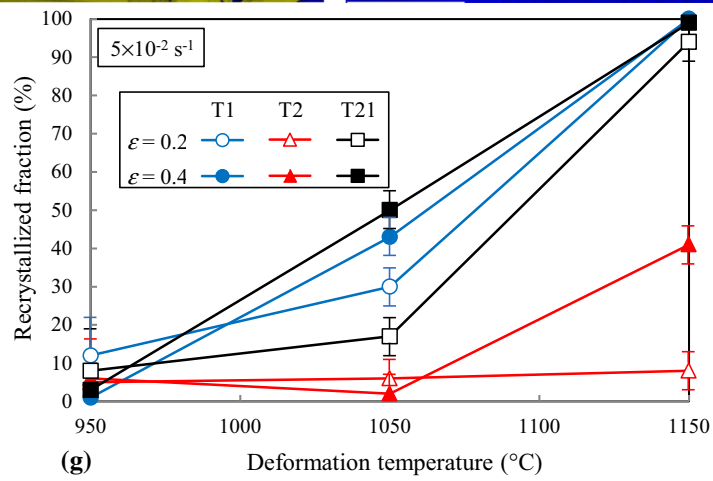
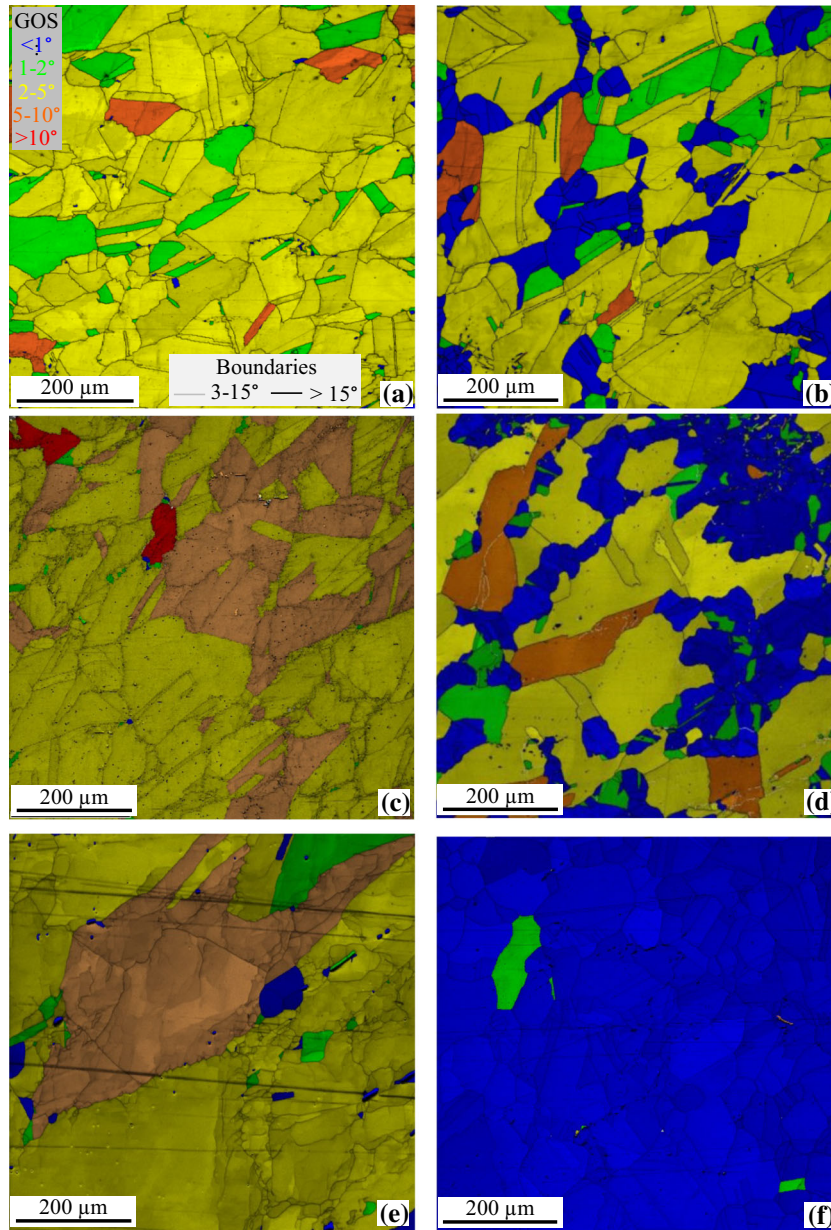
the slower deformation process let enough time for destabilized twin boundaries to migrate and eventually disappear from unrecrystallized grains.

2. T2 microstructure

The recrystallization behavior of T2 is illustrated in Figure 6. In contrast to T1, no serrated grain boundaries were observed in T2 after $\epsilon = 0.2$ whatever the deformation temperature and strain rate, showing a critical deformation beyond 0.2 to initiate the first stages of DRX. As a consequence, no post-DRX could occur and only unrecrystallized grains were found after slow cooling after $\epsilon = 0.2$ (Figure 6(c)). After $\epsilon = 0.4$, serrated grain boundaries were observed at high deformation temperature such as 1423 K (1150 °C), Figure 6(f), and much more scarcely at 1323 K (1050 °C), Figures 6(a) and (d). Even then, the recrystallized fraction after slow cooling did not exceed 0.5 at $5 \times 10^{-2} \text{ s}^{-1}$ (see Figure 6(f) and red triangles in Figure 5(g)). As for T1, due to the lower amount of stored energy, decreasing the strain rate down to $5 \times 10^{-3} \text{ s}^{-1}$ induced a rise of the deformation temperature required to initiate post-DRX; no post-DRX was even observed after slow cooling after $\epsilon = 0.4$ at 1423 K (1150 °C) and $5 \times 10^{-3} \text{ s}^{-1}$. For higher applied strain $\epsilon = 0.8$, serrated grain boundaries were observed at 1323 K (1050 °C) for both strain rates, extensively at $5 \times 10^{-3} \text{ s}^{-1}$ (Figure 6(b)), more scarcely at $5 \times 10^{-2} \text{ s}^{-1}$ (Figure 6(e)). From these results, the bulging mechanism at grain boundaries was still active in the T2 microstructure but required higher amounts of high-temperature strain.

3. T21 microstructure

As illustrated in Figure 7, the recrystallized fraction after deformation at 1323 K (1050 °C) and $5 \times 10^{-2} \text{ s}^{-1}$ followed by slow cooling increased with the applied strain, from 0.15 at $\epsilon = 0.2$ (Figure 7(a)) up to 0.5 at $\epsilon = 0.4$ (Figure 7(b)). Recrystallized fractions were not significantly different from those obtained with the T1 microstructure (see squares in Figure 5(g)). As previously shown for the flow behavior (Figure 2), increasing the grain size from 130 to 280 μm did not affect the microstructural evolution of the matrix either. As for T1, grain boundary serrations as a prelude to DRX and thus to post-DRX were already observed after $\epsilon = 0.2$ at 1323 K (1050 °C). When deformed at 1423 K (1150 °C), the recrystallized fraction reached about 0.9 after slow cooling for both values of applied strain as illustrated in Figure 7(c). Although the grain boundary area per unit volume (and thus the density of nucleation sites) was lower than for T1, new DRX grains grew



rapidly and a homogenous recrystallized microstructure was observed after slow cooling. After deformation at 1323 K (1050 °C), partial post-DRX occurred. Similarly to T1 and T2, no post-DRX occurred after deformation at 1223 K (950 °C). From these results, the post-DRX behavior was thus similar for starting grain sizes of 130 μm (T1) and of 280 μm (T21) as soon as the final preconditioning temperature was the same, namely, 1373 K (1100 °C).

D. Static Phenomena: Microstructural Evolution After Annealing

1. T1 microstructure

Figure 8(a) displays a GOS map after deformation up to $\varepsilon = 0.2$ at 1323 K (1050 °C) and $5 \times 10^{-2} \text{ s}^{-1}$ followed by slow cooling then annealing. The sample was partially recrystallized after slow cooling (Figure 5(b)). SRX involved further growth of post-DRX grains. The recrystallized fraction rose from 0.2 up to 0.75 during annealing. After deformation at 1223 K (950 °C), new grains also nucleated during annealing leading to full recrystallization. For lower amounts of strain (*i.e.*, $\varepsilon = 0.2$) and intermediate deformation temperature of 1323 K (1050 °C), the microstructure after annealing kept some unrecrystallized grains. Figure 8(e) summarizes final recrystallization fractions experimentally measured at $5 \times 10^{-2} \text{ s}^{-1}$ after slow cooling and annealing. When the deformation temperature reached 1423 K (1150 °C), the microstructures were already fully recrystallized after slow cooling. In that case, no further grain evolution was observed between post-DRX and SRX states *i.e.*, no significant grain growth occurred during annealing. Decreasing the strain rate down to $5 \times 10^{-3} \text{ s}^{-1}$ did not influence SRX phenomena but enlarged the deformation temperature range leading to incomplete recrystallization after annealing. However, whatever the strain rate and the deformation temperature, the recrystallized fraction was at least 0.75.

2. T2 microstructure

As shown in Figures 8(b), (d) and (e), SRX of deformed T2 microstructures was restricted to samples severely deformed at lower temperature. Partial SRX was observed after $\varepsilon = 0.4$ at 1223 K (950 °C) and $5 \times 10^{-2} \text{ s}^{-1}$. For the other deformation conditions, the microstructure kept unrecrystallized except for samples strained at 1423 K (1150 °C) where post-DRX had occurred during slow cooling. From TEM observations (Figure 8(d)), unrecrystallized grains exhibited a strongly recovered microstructure.

3. T21 microstructure

Similarly to T1, microstructures after annealing were fully recrystallized for low deformation temperatures (typically, 1223 K (950 °C)) and low amounts of strain ($\varepsilon = 0.2$). As for T1, partial SRX was only observed after $\varepsilon = 0.2$ at 1323 K (1050 °C) and $5 \times 10^{-2} \text{ s}^{-1}$ (Figures 8(c) and (e)). Once more, increasing the initial grain size from 130 to 280 μm did not intrinsically affect static recrystallization mechanisms and kinetics for the

investigated conditions. Note that this finding might be limited to the range of investigated grain sizes, *i.e.*, to very coarse grains.

E. Interactions Between Niobium-Rich Precipitates and Recrystallization Phenomena

From water quenched and slowly cooled samples, undissolved primary carbonitride particles of a few micrometers in size were readily observed both in grains and at grain boundaries. Typical pictures of secondary Nb-rich precipitates are shown in Figure 9. In specimens deformed at 1323 K (1050 °C), $\varepsilon = 0.2$ and water quenched, fine Nb-rich precipitates were readily found, indicating dynamic precipitation during the hot torsion test (Figure 9(b)). Deformed, then slowly cooled down specimens exhibited a heterogeneous spatial distribution of fine Nb-rich precipitates, and a bimodal size distribution with maxima centered about 40 and 200 nm respectively. They were arranged in rows in partially or non-recrystallized microstructures. After slow cooling (*e.g.*, Figures 9(a) and (c)) the finer population of Nb-rich precipitates of 40 nm in size was less predominant than after water quench (*e.g.*, Figure 9(b)) suggesting further growth of these particles during slow cooling. From complementary TEM observations of thin foils, alignments of small precipitates were associated with grain boundaries, subgrain boundaries and dislocation structures as already observed by Barlow *et al.*^[48]

In fully recrystallized specimens that had been deformed at 1423 K (1150 °C) then slowly cooled, no small Nb-rich precipitates were found. Nucleation of these particles during slow cooling thus required a deformed microstructure. On the other hand, a further annealing of these specimens at T_{anneal} again produced homogeneously distributed fine Nb-rich particles (Figure 9(d)), in spite of the low density of potential nucleation sites. The lower solubility of carbon in austenite at low temperature, combined to the low heating rate used in the annealing cycle promoted precipitation.

Nevertheless, for all investigated slow cooling and annealing conditions, the size of Nb-rich precipitates, if any, was at least 40 nm and most frequently, close to 200 nm. In view of their relatively coarse size and their low volume fraction, these particles were probably too coarse to efficiently impede DRX, post-DRX or SRX by Zener pinning,^[20,49] although particles of up to 150 nm in size were found to efficiently pin dislocations and grain boundaries in Mo-free Ni-30Fe-Nb-C alloys.^[43] Therefore, in the following, no grain boundary pinning effect of fine Nb-rich precipitates will be discussed.

IV. DISCUSSION

A. Effect of the Starting Microstructure on the Viscoplastic Behavior Before Recrystallization

From the hot torsion curves (Figure 2(b)), two phenomena characterize the dependence of the

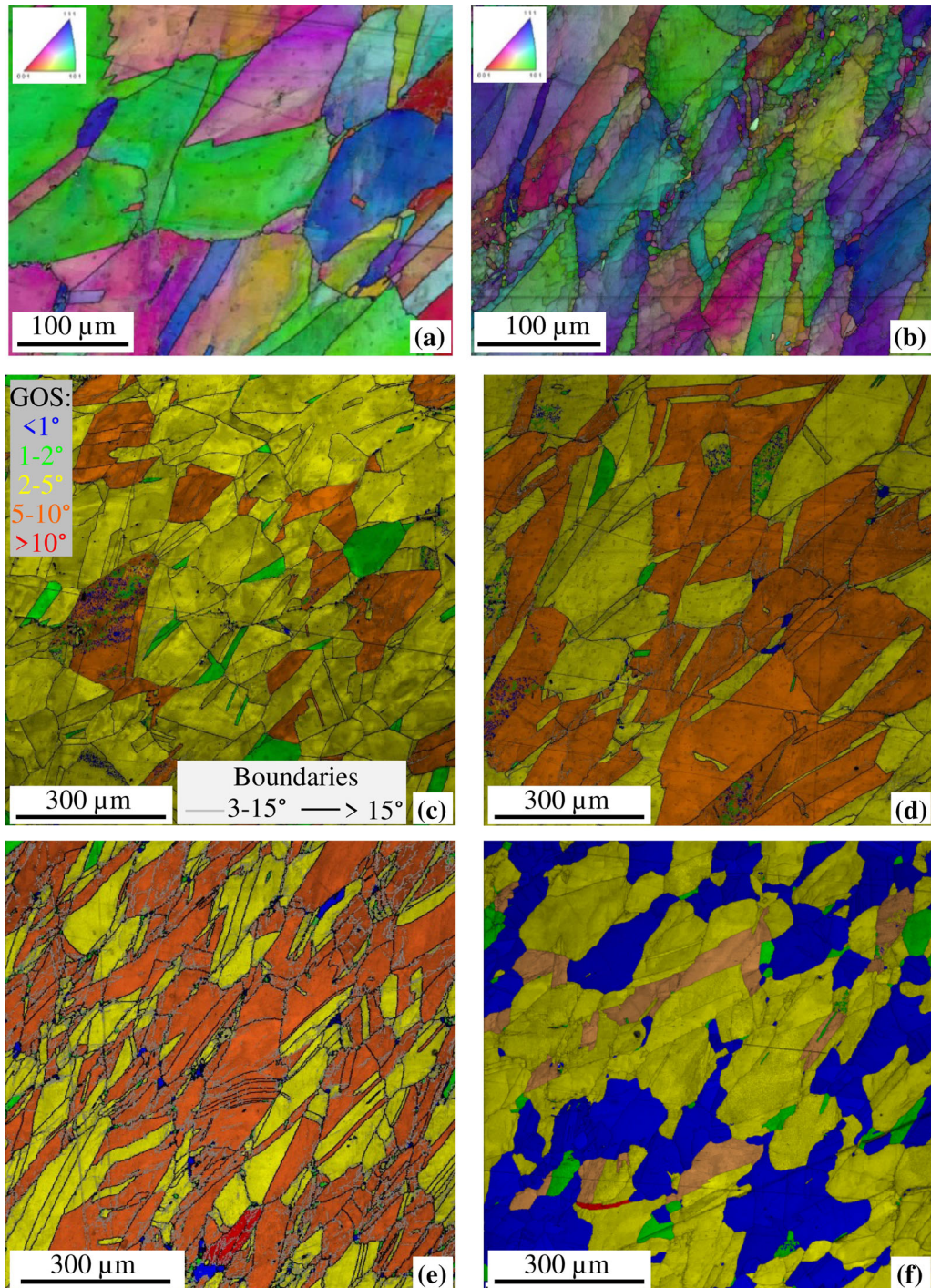


Fig. 6—(a, b) Enlarged views of EBSD maps (pattern quality + IPF) from T2 specimens deformed at 1323 K (1050 °C) (a) up to $\epsilon = 0.4$ at $5 \times 10^{-2} \text{ s}^{-1}$ and (b) up to $\epsilon = 0.8$ at $5 \times 10^{-3} \text{ s}^{-1}$, then slowly cooled. Brighter particles in (b) are primary carbides. (c–f) EBSD pattern quality + GOS maps from T2 specimens deformed at $5 \times 10^{-2} \text{ s}^{-1}$ up to (c) $\epsilon = 0.2$, (d) $\epsilon = 0.4$, (e) $\epsilon = 0.8$ at 1323 K (1050 °C), and (f) $\epsilon = 0.4$ at 1423 K (1150 °C), then slowly cooled.

viscoplastic behavior on the starting microstructure, namely, a higher yield stress for T2 compared to T1 and T21, and higher work hardening ability of T1 and T21 at low strains compared to T2, at least at 1323 K and 1423 K (1050 °C and 1150 °C). The contribution of work hardening and of DRV to the flow curves was quantified by using a macroscopic model based on dislocation

densities, namely, the Estrin–Mecking model.^[50] In this model, the dislocation density, ρ , can be expressed as a function of strain, ϵ , using the following evolutionary equation:

$$\frac{d\rho}{d\epsilon} = h - r\rho. \quad [2]$$

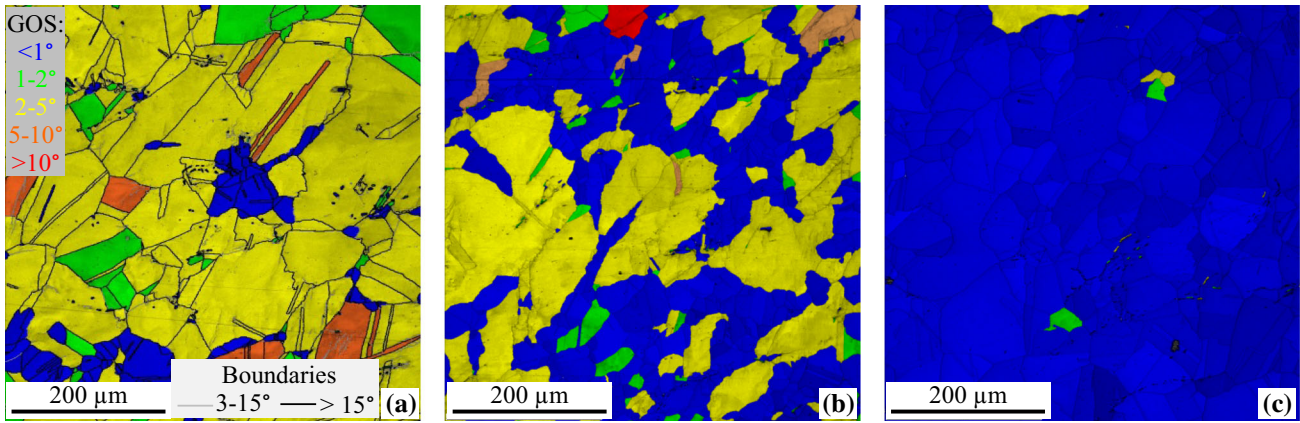


Fig. 7—EBSD pattern quality + GOS maps showing post-DRX of T21 specimens deformed at $5 \times 10^{-2} \text{ s}^{-1}$ up to (a) $\varepsilon = 0.2$ and (b) $\varepsilon = 0.4$ at 1323 K (1050 °C), and (c) up to $\varepsilon = 0.4$ at 1423 K (1150 °C), then slowly cooled.

In Eq. [2], h is the athermal work-hardening rate that represents stored dislocations and r characterizes the dynamic recovery. Both values depend on the deformation temperature and strain rate. As shown in Reference 51, for an isothermal test at constant strain rate, the value of r can be derived from the flow curve by using the following equations:

$$\sigma^2 = \sigma_{\text{sat}}^2 - (\sigma_{\text{sat}}^2 - \sigma_0^2) \exp(-r\varepsilon). \quad [3]$$

In Eq. [3], σ_0 and σ_{sat} are the value of flow stress, respectively, for $\varepsilon = 0$ and for $\varepsilon \rightarrow +\infty$ (without taking recrystallization-induced softening into account). It then comes:

$$\sigma \frac{d\sigma}{d\varepsilon} = \frac{1}{2} r \sigma_{\text{sat}}^2 - \frac{1}{2} r \sigma^2. \quad [4]$$

From Eq. [4], for each hot torsion curve, it is possible to determine the value of r from a $\sigma \frac{d\sigma}{d\varepsilon}$ vs σ^2 plot. These plots were drawn from the curves of Figure 2, by applying a gliding average noise reduction to these curves in order to calculate the work hardening rate, $d\sigma/d\varepsilon$. A polynomial fit of flow curves as in Reference 51 was not possible, as the curves were not determined up to the steady-state, so that fitting a polynomial on available data would have introduced a high uncertainty on the curvature of the curves and on the resulting values of r and h . In the work hardening rate vs flow stress curves (Figure 10(a)), the peak stress, σ_p is given by the value of stress once the work-hardening rate reaches zero *i.e.* by the intersection of the curves of Figure 10(a) with the ($\sigma = 0$) axis. On the other hand, σ_c and corresponding strain, ε_c are given by the inflexion point (indicated with a star in Figure 10(a)).

The intersection of the tangent to the curve at $\sigma = \sigma_c$ (thin dashed lines in Figure 10(a)) and the ($\sigma = 0$) axis gives the value of σ_{sat} ^[51] (open circles in Figure 10(a)). In the present work, the $\sigma \frac{d\sigma}{d\varepsilon}$ vs σ^2 plots of Figure 10(b) were not strictly linear, so that their slope ($-0.5r$ in view of Eq. [4]) was taken for strain values approaching ε_c , but

still below ε_c , as in Reference 51. This corresponds to the bottom, straight part of the curves in Figure 10(b). For some tests, the value of r could not be determined with acceptable accuracy, due to a high noise level introduced by the calculation of the work-hardening rate and to the unusual waviness of the curves obtained at $5 \times 10^{-1} \text{ s}^{-1}$, probably owing to a slight misalignment of the load lines in those tests (Figure 2(a)). When available, the values of h were derived from those of r by using the following equation^[51]:

$$h = \frac{r \sigma_{\text{sat}}^2}{(\alpha \mu b)^2}. \quad [5]$$

The value of parameter α was set to 1 as in Reference 52 and that of Burgers vector b was set to 2.5×10^{-10} m. The shear modulus, μ , was taken from the temperature dependency reported by Reference 53 for 316-type stainless steels.

From replicate calculations on typical flow curves, the relative uncertainty on the values of r and h was estimated to be ± 5 and ± 10 pct, respectively, close to the value of ± 6 pct reported by Reference 51. The results are reported in Figure 11, together with literature data. Note that the values from Reference 51 for low alloy steels could not be added to Figure 11 because the individual values of Z were not given. Nevertheless, the values of r reported in Reference 51 ranged between 3 and 10 and decreased with increasing Z , while the values of h increased with increasing Z , from $2 \times 10^{14} \text{ m}^{-2}$ up to $2 \times 10^{15} \text{ m}^{-2}$ for peak stresses between 80 and 130 MPa. By taking the abovementioned values of α , μ , and b , estimates of h from the present work ranged between 3.0×10^{14} and 2.4×10^{15} , in excellent agreement with Reference 51 and with literature results reported in Figure 11.

From Figure 11, the values of h and r , even if scattered, were not correlated to the starting microstructure, consistently with the similar shapes of the curves in Figure 10, especially close to $\varepsilon = \varepsilon_c$. Moreover, they well agree with those reported for a high-purity Fe-18Cr-12Ni,^[52,54] in particular for the coarser grain size, but not with those of h reported by Reference 55 for

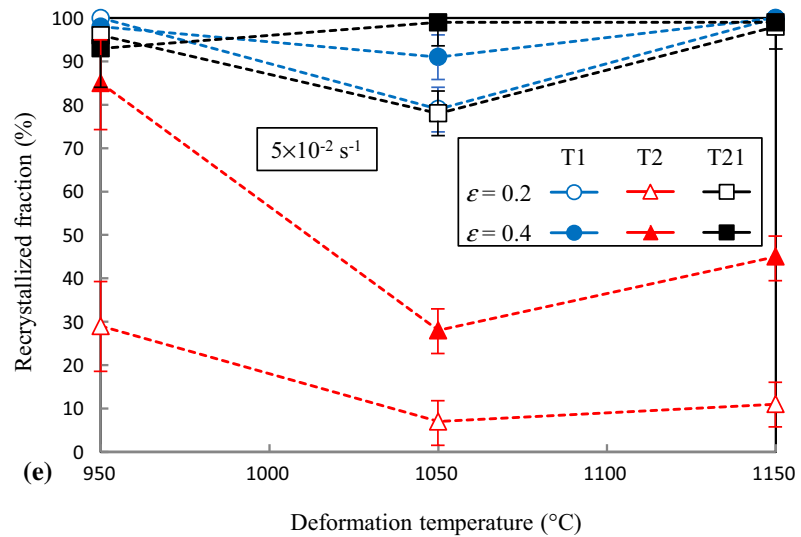
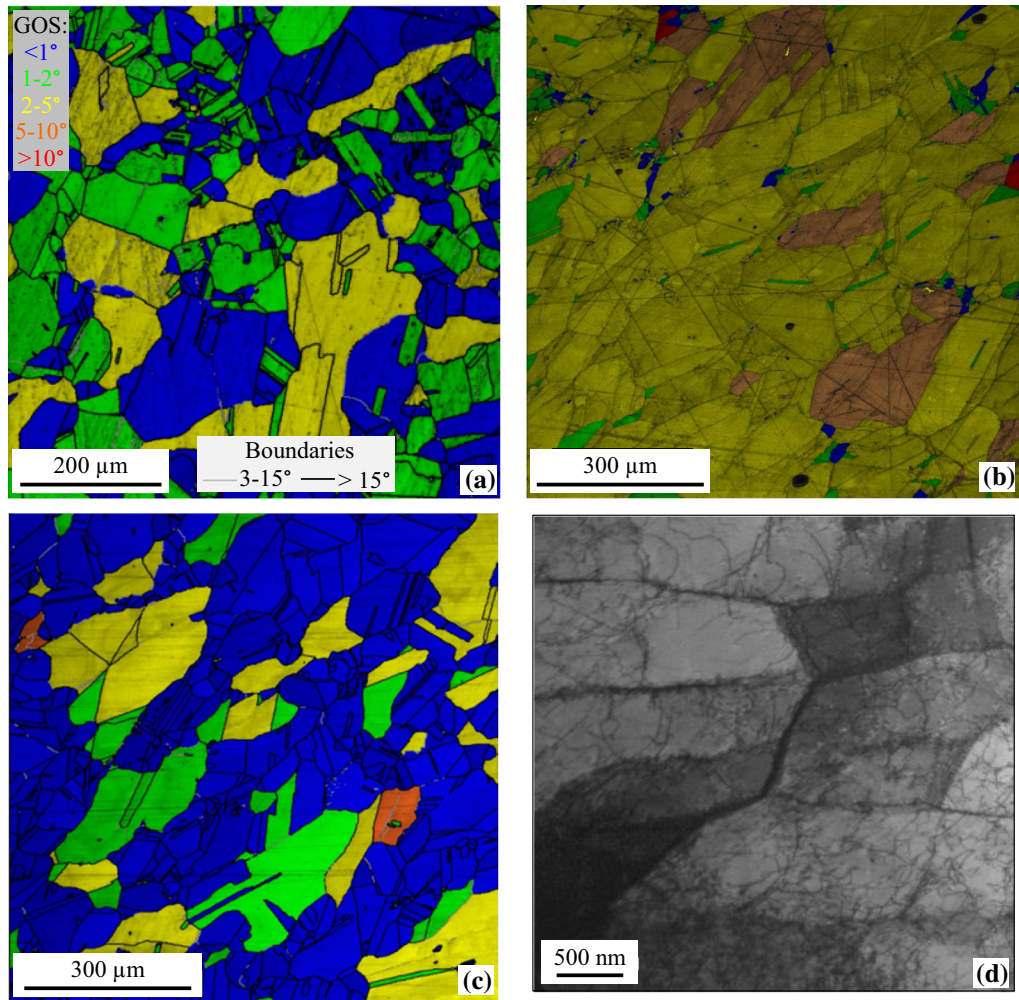


Fig. 8—EBSD pattern quality + GOS maps from (a) a T1, (b) a T2, and (c) a T21 specimen deformed up to $\epsilon = 0.2$ at 1323 K (1050 °C) and $5 \times 10^{-2} \text{ s}^{-1}$ followed by slow cooling and annealing. (d) TEM bright field micrograph of the same T2 specimen showing extensive recovery. (e) Recrystallized fraction experimentally measured after deformation at $5 \times 10^{-2} \text{ s}^{-1}$ followed by slow cooling and annealing.

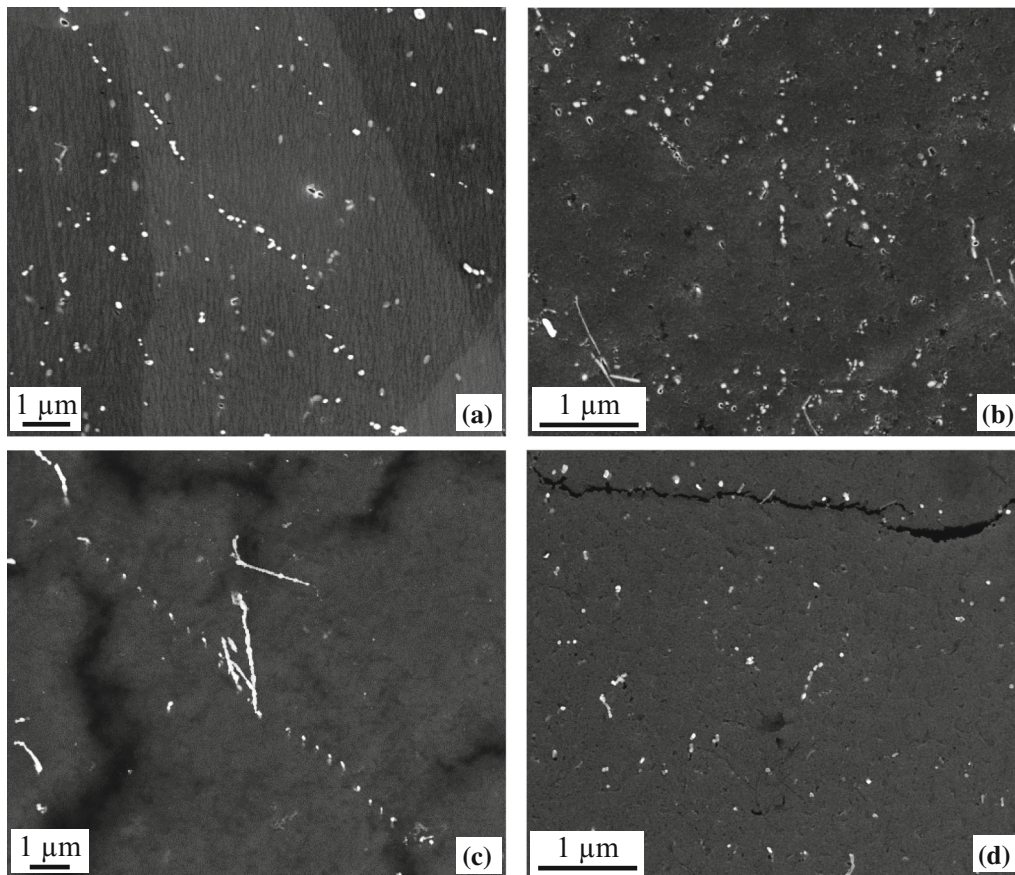


Fig. 9—SEM observation of fine Nb-rich precipitates on extractive replicas taken after hot torsion (*a, b, c*) at 1323 K (1050 °C) and (*d*) at 1423 K (1150 °C), $\varepsilon = 0.2$ at $5 \times 10^{-2} \text{ s}^{-1}$. (*a*) T1 microstructure, slowly cooled; (*b*) T2 microstructure, water quenched; (*c*) T21 microstructure, slowly cooled. (*d*) Fine Nb-rich precipitates in the T1 microstructure after hot torsion at 1423 K (1150 °C), followed by slow cooling and annealing.

microalloyed steels, yet obtained for lower values of the Zener parameter. The values of r are also close to the range reported by Reference 5 on a Mn- and Mo-bearing austenitic stainless steel. The values of h and r also well agree with ranges reported for coarse-grained Ni-Nb alloys containing up to 1 wt pct Nb.^[56] Altogether, this tends to show that the difference in starting microstructure, as well as differences in austenitic stainless steel chemistry do not affect the general trends of the macroscopic flow behavior. By further considering the curves of Figure 2, the effect of the starting microstructure is mostly sensible at the very beginning of the curves, namely, for strains lower than 0.1 and especially for strains lower than 0.05. The above model, mainly designed to represent the overall DRV behavior, the onset of recrystallization and further grain growth and even the steady-state microstructure and flow, does not capture the effects of preconditioning conditions on further recrystallization, especially, on post-dynamic and static phenomena in the present case. These effects seem to concentrate on the beginning of viscoplastic deformation.

As shown by the similar flow curves of T1 and T21, the (coarse) grain size is not a relevant parameter to characterize the effect of the starting microstructure. For these coarse, well recrystallized starting microstructures,

incipient viscoplastic flow relies on activation of dislocation sources. In fact, these microstructures contain a low density of obstacles to dislocation motion, namely, less than 1 pct coarse delta ferrite, few coarse primary niobium-rich carbonitrides (no secondary Nb-rich precipitate was found either in replicas or in thin foils after the solutionizing step of Figure 1 followed by water quenching), and a limited density of grain boundaries. Even if present, bulk solid solution strengthening by Nb atoms or Nb-rich clusters as reviewed in Reference 22 probably does not explain the higher yield stress and lower work hardening rate found in T2 at low strains. The yield point found at higher temperatures, in particular for the T2 microstructure, suggested that activation of dislocation sources was actually difficult. As these sources were probably mainly at grain boundaries, the effect of the starting microstructure probably relied on what happened close to grain boundaries at the beginning of hot deformation.

B. Effect of the Starting Microstructure on Further Microstructural Evolution Close to Grain Boundaries

During preconditioning, grain boundaries may be pinned by Nb-rich precipitates or by solute drag, inhibiting their migration during thermomechanical

treatments.^[20,57] Owing to the high preconditioning and solutionizing temperatures used in this work [1373 K to 1473 K (1100 °C to 1200 °C)], all *secondary* Nb-rich

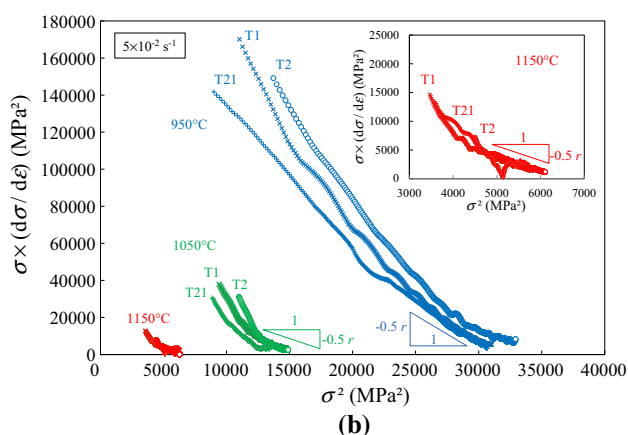
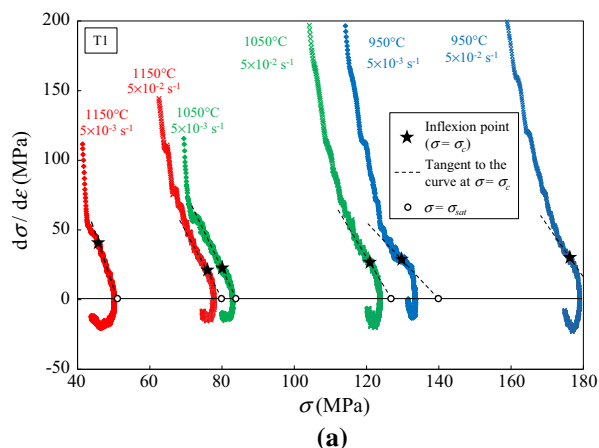


Fig. 10—Identification of macroscopic work-hardening and recovery parameters. (a) Representative work-hardening rate vs stress curves, here for the T1 microstructure at two strain rates. The value of parameter r is two times the opposite of the slope of the curves in (b) (here, for the three microstructures deformed at $5 \times 10^{-2} \text{ s}^{-1}$) as evaluated just before reaching $\sigma = \sigma_c$ (here, straight bottom part of the curves, when available).

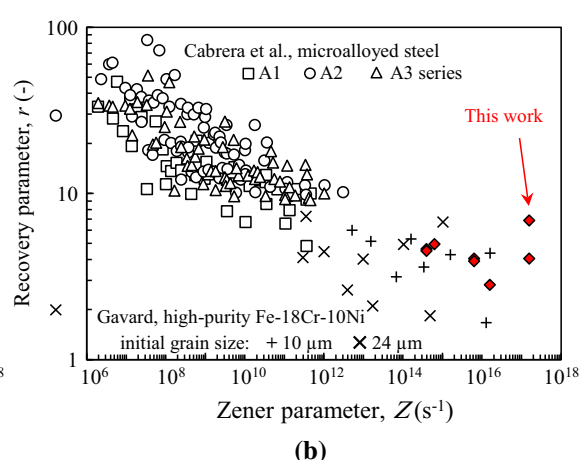
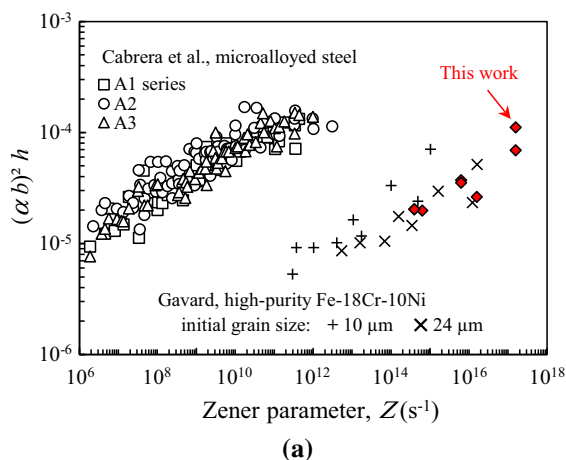


Fig. 11—Comparison of (a) work hardening and (b) dynamic recovery parameters to those reported on a microalloyed steel and on a high-purity Fe-18Cr-10Ni steel (Ref. [52]; chemistry in Ref. [54]).

particles were dissolved during the solutionizing stage of the torsion tests, as stated previously. Some additional dissolution of *primary* Nb-rich carbonitrides could have occurred during preconditioning, in particular at 1473 K (1200 °C), both for T2 and T21, due to the higher solubility of Nb and C atoms in the matrix with increasing the preconditioning temperature. Note that primary carbides being very scarcely distributed and mainly located at grain boundaries after the preconditioning treatment, their contribution to recrystallization by particle-stimulated nucleation, as reported in *e.g.*, References 43 and 58 could not be isolated but is probably not predominant. On the other hand, solute niobium (and probably associated carbon) atoms were found to segregate at grain boundaries, as shown by the STEM-EDS profile of Figure 12 for the T2 microstructure. A similar result was obtained for the T1 microstructure. Some segregation of Mo was occasionally found. The standardless analysis method used here did not allow quantitative comparison of grain boundary segregation levels between T1 and T2 microstructures, so that the amounts of Nb atoms both at the grain boundaries and close to them could not be accurately quantified and compared. The low fraction of Nb atoms might make it difficult to get an accurate quantification of the solid solution chemistry at grain boundaries, even at a very local scale accessible with *e.g.*, atom probe tomography. In the present work, strain-induced recrystallization involved the progressive lattice rotation of subgrains adjacent to pre-existing grain boundaries; this mechanism was mostly reported in materials in which solute drag affects dislocation motion.^[8] As such, segregation of Nb atoms at (or close to) grain boundaries could have impacted the DRV behavior close to grain boundaries and thus the DRX kinetics.

As the grain size of the T21 microstructure was slightly higher than that of T2, together with a yield stress comparable to that of T1, the viscoplastic flow behavior of the T2 microstructure is not directly linked to its grain size. It might be linked to a difference in solute segregation close to grain boundaries, again not due to the grain size itself (*i.e.*, to the grain boundary

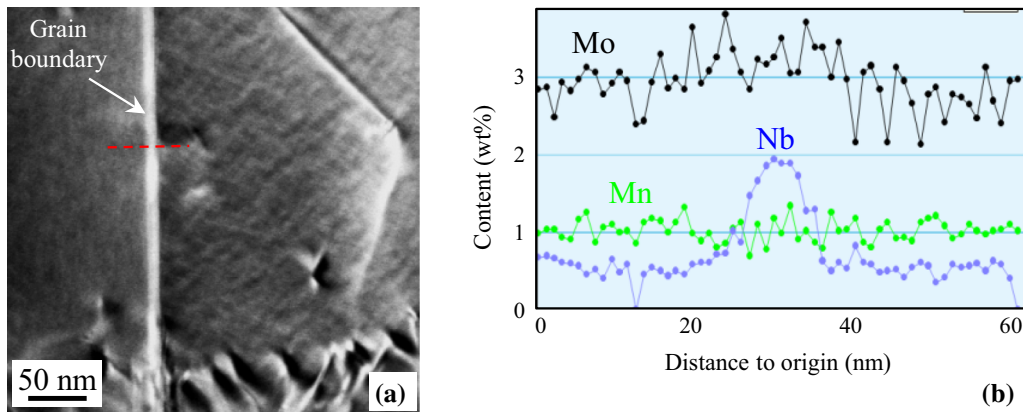


Fig. 12—(a) STEM observation of undeformed T2 microstructure, (b) EDS analysis across a grain boundary (dashed line in a).

area per unit volume) but to the finishing temperature of preconditioning. The difference in incipient flow and further recrystallization behavior between T2 and T21 suggests that during the final isothermal holding at 1373 K (1100 °C) used to prepare T21, slower grain growth (from 250 μm in T2 up to 280 μm in T21 in average, see Table I) could have modified solute drag conditions and local gradients in Nb content close to grain boundaries, going back to the situation encountered next to grain boundaries when preparing the T1 microstructure. Niobium atoms did not have time to diffuse in the lattice over significant distances during the torsion test, which in most of the selected conditions lasted for less than one minute. From the DICTRA-MOBFE4 mobility database, the lattice diffusion distance of Nb atoms during holding at 1200 °C for 1 hour is less than 20 μm ; during a typical torsion test (950 °C to 1100 °C, for up to 1 min) it drops down to less than 0.5 μm . As for carbon atoms, lattice diffusion distances were estimated by using the DICTRA-MOBFE4 database together with various combinations of amounts of C, N, and Nb atoms in the range reported for the chemistry of the material under study. Typical lattice diffusion distances of carbon atoms for 10 seconds (resp. 1 min) are 8 (19) μm at 950 °C, 21 (51) μm at 1100 °C, and 36 (87) μm at 1200 °C, respectively, yet not taking any trapping at grain boundaries into account. In summary, the chemistry at grain boundaries (*i.e.* segregation levels) and also close to grain boundaries (in regions that could be affected by the bulging phenomenon) could still have remained stable during the first seconds of the torsion test itself. Consequently, the particular chemistry at grain boundaries resulting from preconditioning could have generated a difference in the deformation microstructure close to boundaries at incipient plastic deformation. This difference could have persisted even at higher strains, even if the macroscopic behavior did not strongly depend on the starting microstructure. This is suggested by the higher resistance of T2 to high-temperature bulging of grain boundaries.

From the results obtained after slow cooling and after further annealing, the difference in microstructure (and possibly in chemistry) close to grain boundaries further impacted the post-dynamic and static recrystallization

behavior. Increasing the preconditioning temperature from 1373 K (1100 °C) up to 1473 K (1200 °C) decreased the work hardening ability at low strains. Partial dissolution of coarse Nb-rich precipitates during preconditioning may have led to an overall increase in niobium and carbon solute contents. Even if solute drag tended to concentrate Nb (and possibly C) atoms at grain boundaries (Figure 12), grain interiors were probably also affected, consistently with the high diffusion distance of C atoms during the preconditioning treatment. Namely, Figure 7 shows that cell structures were locally present in the T2 microstructure strained up to $\varepsilon = 0.2$ at 1323 K (1050 °C) at $5 \times 10^{-2} \text{ s}^{-1}$ and then water quenched. After slow cooling, the microstructure was fully recovered and further annealing did not affect the recovered microstructure (Figure 10). Even if not very sensitive in macroscopic curves, recovery was strongly promoted throughout the entire volume by a higher preconditioning temperature. This behavior might suggest an increase in SFE due to the higher amounts of niobium and (or) carbon atoms in solid solution (or at dislocation cores), leading to lower amounts of stored energy and more difficult post-DRX and SRX (Figure 10). Such an increase in SFE of austenitic stainless steels due to Nb atoms, at least at room temperature, has already been reported in References 59 and 60.

V. CONCLUSIONS

Hot torsion tests on a coarse-grained (Mo + Nb) bearing, so-called “316Nb” austenitic stainless steel, followed by cooling and further annealing, as well as microstructural examinations led to the following conclusions:

- Dynamic recrystallization mainly started from boundaries, by a bulging mechanism associated to subgrain formation close to grain boundaries. A specific mechanism was evidenced at annealing twin boundaries, explaining their progressive elimination in many unrecrystallized grains during hot deformation. Both the occurrence of dynamic recovery,

coarse initial grain size and solute drag effects limited dynamic recrystallization in the investigated conditions. Post-DRX occurred by rapid growth of nuclei, and was affected by deformation conditions. SRX involved further growth of post-DRX grains and nucleation of new grains.

- A strong effect of the starting microstructure was found; it was independent of the grain size in the range 130 to 280 μm (but this might not be valid for finer grain sizes). It was attributed to additional Nb atoms that were made available by some dissolution of primary Nb-rich carbides formed at the end of solidification. The relevant processing parameter was shown to be the final “preconditioning” temperature used to prepare the starting microstructure.
- Increasing the final preconditioning temperature led to higher yield stress, lower work hardening at low strains but did not affect the viscoplastic behavior at high strains (close to the onset of recrystallization). In their present state, macroscopic models could not capture the effect of the starting microstructure on the recrystallization behavior in the investigated conditions.
- Dynamic recrystallization, but also post-dynamic and static recrystallization phenomena were strongly affected by the microstructure close to grain boundaries. Differences in solute drag conditions during final grain growth could have impacted local dynamic recovery close to grain boundaries, and thus further recrystallization phenomena. In addition, released Nb or C atoms also seemed to have affected the overall dynamic recovery behavior (and possibly the stacking fault energy), and thus the driving force available for further recrystallization.

ACKNOWLEDGMENTS

The authors wish to thank Dr. V. Esin and Mr. N. Cliche (Centre des Matériaux) for their kind help, especially for DICTRA calculations (V.E.) and fruitful discussions about viscoplastic flow modeling (N.C.).

REFERENCES

1. B. Guo, H. Ji, X. Liu, L. Gao, R. Dong, M. Jin, and Q. Zhang: *J. Mater. Eng. Perform.*, 2012, vol. 21, pp. 1455–61.
2. A. Perron, C. Toffolon-Masclat, X. Ledoux, F. Buy, T. Guilbert, S. Urvoy, S. Bosonnet, B. Marini, F. Cortial, G. Texier, C. Harder, V. Vignal, Ph. Petit, J. Farré, and E. Suzon: *Acta Mater.*, 2014, vol. 79, pp. 16–29.
3. L. Sun, K. Muszka, B.P. Wynne, and E.J. Palmiere: *Mater. Sci. Eng. A*, 2013, vol. A568, pp. 160–70.
4. A. Dehghan-Manshadi, M.R. Barnett, and P.D. Hodgson: *Metall. Mater. Trans. A*, 2008, vol. 39A, pp. 1371–81.
5. R.C. Souza, E.S. Silva, A.M. Jorge, Jr., J.M. Cabrera, and O. Balancin: *Mater. Sci. Eng. A*, 2013, vol. A582, pp. 96–107.
6. R.E. Schramm and R.P. Reed: *Metall. Mater. Trans. A*, 1975, vol. 6A, pp. 1345–51.
7. E.J. Giordani, A.M. Jorge, Jr., and O. Balancin: *Scripta Mater.*, 2006, vol. 55, pp. 743–46.
8. F.J. Humphreys and M. Hatherly: *Recrystallization and Related Annealing Phenomena*, 2nd ed., Elsevier Science, Boston, 2004.
9. T. Sakai and J.J. Jonas: *Acta Metall.*, 1984, vol. 32, pp. 189–209.
10. A.N. Belyakov: *Phys. Metals Metallogr.*, 2009, vol. 108, pp. 390–400.
11. A.S. Taylor and P.D. Hodgson: *Mater. Sci. Eng. A*, 2011, vol. A528, pp. 3310–20.
12. S. Venegopal, S.L. Mannan, and Y.V.R.K. Prasad: *Metall. Mater. Trans. A*, 1992, vol. 23A, pp. 3093–3103.
13. D. Ohadi, M.H. Parsa, and H. Mirzadeh: *Mater. Sci. Eng. A*, 2013, vol. A565, pp. 90–95.
14. R.M. Latanision and A.W. Ruff, Jr.: *Metall. Trans.*, 1971, vol. 2, pp. 505–09.
15. C.C. Bampton, I.P. Jones, and M.H. Loretto: *Acta Metall.*, 1978, vol. 26, pp. 39–51.
16. L. Rémy, A. Pineau, and B. Thomas: *Mater. Sci. Eng.*, 1978, vol. 36, pp. 47–63.
17. J.C. Bavay: *Aciers inoxydables austénitiques. Les aciers inoxydables in Les éditions de physique*, P. Lacombe, B. Baroux, and G. Béranger, eds., Les Ulis, France, 1990, pp. 567–610.
18. A. Sandberg and R. Sandström: *Mater. Sci. Technol.*, 1986, vol. 2, pp. 917–25.
19. F. Xiao, Y.B. Cao, G.Y. Qiao, X.B. Zhang, and B. Liao: *J. Iron Steel Res. Int.*, 2012, vol. 19, pp. 52–56.
20. A.G. Kostryzhev, A. Al Shahrani, C. Zhu, S.P. Ringer, and E.V. Pereloma: *Mater. Sci. Eng. A*, 2013, vol. A581, pp. 16–25.
21. C.R. Hutchinson, H.S. Zurob, C.W. Sinclair, and Y.J.M. Bréchet: *Scripta Mater.*, 2008, vol. 59, pp. 635–37.
22. M.C. Mataya, C.A. Perkins, S.W. Thompson, and D.K. Matlock: *Metall. Mater. Trans. A*, 1996, vol. 27A, pp. 1251–66.
23. C. Rehr, S. Kleber, O. Renk, and R. Pippan: *Mater. Sci. Eng. A*, 2012, vol. A540, pp. 55–62.
24. A. Hermant, E. Suzon, J. Bellus, P. Petit, F. Cortial, A.-F. Gourgues: Hot deformation behavior and recrystallization mechanisms in a niobium stabilized austenitic stainless steel. Proceedings of the 6th Int. Conf. On Recrystallization and Grain Growth, Pittsburgh, 17–21 July, 2016, ed. E. Holm, S. Farjami, P. Manohar, G. Rohrer, A. Rollett, D. Slorovitz, H. Weiland, TMS, 2016, pp. 209–14.
25. D.S. Fields and W.A. Backofen: *Proc. Am. Soc. Test. Mater.*, 1957, vol. 57, pp. 1259–72.
26. D.P. Field, L.T. Bradford, M.M. Nowell, and T.M. Lillo: *Acta Mater.*, 2007, vol. 55, pp. 4233–41.
27. S. Mandal, A.K. Bhaduri, and V. Subramanya Sarma: *Metall. Trans. A*, 2011, vol. 42A, pp. 1062–72.
28. S.-I. Kim, Y. Lee, and B.-L. Jang: *Mater. Sci. Eng. A*, 2003, vol. A357, pp. 235–39.
29. G. Angella, B.P. Wynne, W.M. Rainforth, and J.H. Beynon: *Mater. Sci. Eng. A*, 2008, vol. A475, pp. 257–67.
30. R. Fu, F. Li, F. Yin, D. Feng, Z. Tian, and L. Chang: *Mater. Sci. Eng. A*, 2015, vol. A638, pp. 152–64.
31. Z. Wenhui, S. Shuhua, Z. Deli, W. Baozhong, W. Zhenhua, and F. Wantang: *Mater. Des.*, 2011, vol. 32, pp. 4173–79.
32. N.D. Ryan and H.J. McQueen: *J. Mater. Proc. Technol.*, 1993, vol. 36, pp. 103–23.
33. D. Jorge-Badiola, A. Iza-Mendia, and I. Gutiérrez: *Mater. Sci. Eng. A*, 2005, vol. A394, pp. 445–54.
34. C.M. Sellars and W.J. McTegart: *Acta Metall.*, 1996, vol. 14, pp. 1136–38.
35. S. Wang, M. Zhang, H. Wu, and B. Yang: *Mater. Charact.*, 2016, vol. 118, pp. 92–101.
36. W. He, J. Liu, H. Chen, and H. Guo: *Adv. Mater. Res.*, 2010, vols. 139–141, pp. 516–19.
37. A. Belyakov, H. Miura, and T. Sakai: *Mater. Sci. Eng. A*, 1998, vol. A255, pp. 139–47.
38. N.D. Ryan and H.J. McQueen: *Can. Metall. Q.*, 1990, vol. 29, pp. 147–52.
39. A. Belyakov, T. Sakai, H. Miura, and R. Kaibyshev: *ISIJ Int.*, 1999, vol. 39, pp. 592–99.
40. D. Samantaray, S. Mandal, C. Phaniraj, and A.K. Bhaduri: *Mater. Sci. Eng. A*, 2011, vol. A528, pp. 8565–72.
41. N. Dudova, A. Belyakov, T. Sakai, and R. Kaibyshev: *Acta Mater.*, 2010, vol. 58, pp. 3624–32.
42. M.J. Luton and C.M. Sellars: *Acta Metall.*, 1969, vol. 17, pp. 1033–43.

43. P. Mannan, G. Casillas, and E.V. Pereloma: *Mater. Sci. Eng. A*, 2017, vol. A700, pp. 116–31.
44. D. Samantaray, S. Mandal, V. Kumar, S.K. Albert, A.K. Bhaduri, and T. Jayakumar: *Mater. Sci. Eng. A*, 2012, vol. A552, pp. 236–44.
45. D. Ponge and G. Gottstein: *Acta Mater.*, 1998, vol. 46, pp. 69–80.
46. M. Zouari, N. Bozzolo, and R.E. Logé: *Mater. Sci. Eng. A*, 2015, vol. A655, pp. 408–24.
47. D.G. Brandon: *Acta Metall.*, 1966, vol. 14, pp. 1479–84.
48. C.Y. Barlow, B. Ralph, B. Silverman, and A.R. Jones: *J. Mater. Sci.*, 1979, vol. 14, pp. 423–30.
49. M.B.R. Silva, J. Gallego, J.M. Cabrera, O. Balancin, and A.M. Jorge, Jr.: *Mater. Sci. Eng. A*, 2015, vol. A637, pp. 189–200.
50. Y. Estrin and H. Mecking: *Acta Mater.*, 1984, vol. 32, pp. 57–70.
51. J.J. Jonas, X. Queleñec, L. Jiang, and E. Martin: *Acta Mater.*, 2009, vol. 57, pp. 2748–56.
52. L. Gavard: Recristallisation dynamique d'aciers inoxydables austénitiques de haute pureté (Dynamic recrystallization of high-purity austenitic stainless steels), Ph.D. Dissertation, Institut National Polytechnique de Grenoble, France, 2001. Manuscript (in French) available from following URL: http://www.iaea.org/inis/collection/NCLCollectionStore/_Public/33/021/33021356.pdf (as on 28 February 2018).
53. H.J. Frost and M.F. Ashby: *Deformation-mechanism maps*, Pergamon Press, Oxford, 1982 (Chapter 8).
54. M. El Wahabi, L. Gavard, F. Montheillet, J.M. Cabrera, and A.M. Prado: *Acta Mater.*, 2005, vol. 53, pp. 4605–12.
55. J.M. Cabrera, A. Al Omar, J.J. Jonas, and A.M. Prado: *Metall. Mater. Trans. A*, 1998, vol. 28A, pp. 2233–44.
56. N. Matougui, D. Piot, M.L. Fares, F. Montheillet, and S.L. Semiatin: *Mater. Sci. Eng. A*, 2013, vol. A586, pp. 350–57.
57. L.Q. Ma, Z.Y. Liu, S.H. Jiao, X.Q. Yuan, and D. Wu: *J. Iron Steel Res. Int.*, 2008, vol. 15 (3), pp. 31–36.
58. E.V. Pereloma, P. Mannan, G. Casillas, and A.A. Saleh: *Mater. Charact.*, 2017, vol. 125, pp. 94–98.
59. L.G. Martinez, K. Imakuma, and A.F. Padilha: *Steel Res.*, 1992, vol. 63, pp. 221–23.
60. L. Vitos, J.-O. Nilsson, and B. Johansson: *Acta Mater.*, 2006, vol. 54, pp. 3821–26.